HHS Public Access

Author manuscript

Ann Biomed Eng. Author manuscript; available in PMC 2019 November 01.

Published in final edited form as:

Ann Biomed Eng. 2018 November ; 46(11): 1938–1950. doi:10.1007/s10439-018-2086-7.

Immuno-Driven and Mechano-Mediated Neotissue Formation in Tissue Engineered Vascular Grafts

J.M. Szafron[#1], **R. Khosravi**[#1], **J. Reinhardt**[2], **C.A. Best**[2], **M.R. Bersi**[1], **Tai Yi**[2], **C.K. Breuer**[2], and **J.D. Humphrey**[1,3]

[1]Department of Biomedical Engineering, Yale University, New Haven, CT

[2]Center for Regenerative Medicine, The Research Institute at Nationwide Children's Hospital, Columbus, OH

[3]Vascular Biology and Therapeutics Program, Yale School of Medicine, New Haven, CT

[#] These authors contributed equally to this work.

Abstract

In vivo development of a neovessel from an implanted biodegradable polymeric scaffold depends on a delicate balance between polymer degradation and native matrix deposition. Studies in mice suggest that this balance is dictated by immuno-driven and mechanotransduction-mediated processes, with neotissue increasingly balancing the hemodynamically induced loads as the polymer degrades. Computational models of neovessel development can help delineate relative time-dependent contributions of the immunobiological and mechanobiological processes that determine graft success or failure. In this paper, we compare computational results informed by long-term studies of neovessel development in immuno-compromised and immuno-competent mice. Simulations suggest that an early exuberant inflammatory response can limit subsequent mechano-sensing by synthetic intramural cells and thereby attenuate the desired long-term mechano-mediated production of matrix. Simulations also highlight key inflammatory differences in the two mouse models, which allow grafts in the immuno-compromised mouse to better match the biomechanical properties of the native vessel. Finally, the predicted inflammatory time courses revealed critical periods of graft remodeling. We submit that computational modeling can help uncover mechanisms of observed neovessel development and improve the design of the scaffold or its clinical use.

Keywords

neovessel; wall stress; mechanosensing; inflammation; poly(glycolic acid)

Address for Correspondence: J.D. Humphrey, Ph.D., Department of Biomedical Engineering, Yale University, New Haven, CT 06520, jay.humphrey@yale.edu.

Conflicts of Interest

None.

Introduction

Recent clinical trials evaluating a tissue engineered vascular graft (TEVG) in extra-cardiac Fontan procedures to palliate congenital single ventricle anomalies employed a biodegradable polymeric scaffold, seeded with autologous bone marrow derived mononuclear cells, that was implanted to connect the inferior vena cava to the pulmonary artery. As the component polymers – a poly(glycolic acid) felt (PGA) and a poly(ε-caprolactone and L-lactide) sealant (P(CL/LA)) – degraded, host vascular cells invaded the scaffold and produced neotissue, thus resulting in the first tissue engineered neovessel having growth capacity. Although there was neither mortality nor severe morbidity due to graft-related causes in any of the initial 25 patients, graft stenosis requiring angioplasty manifested in 24% of these cases[6,14]. To better understand and ultimately to improve this promising TEVG, considerable effort subsequently turned toward mouse models wherein one can study more carefully the molecular, cellular, and biomechanical mechanisms of neovessel development. In the absence of a mouse model of single ventricle disease, attention focused on an infrarenal inferior vena cava (IVC) interposition graft model that mimics blood pressures found in the Fontan circulation.

The mouse IVC model revealed two seminal findings. First, seeded bone marrow derived cells do not differentiate into the matrix producing cells that are essential for neotissue formation; rather, through paracrine signaling, the bone marrow derived cells recruit host monocytes which in turn recruit native synthetic vascular cells[34]. Second, stenosis occurs more frequently in unseeded (68%) than seeded (32%) grafts, suggesting that the bone marrow derived cells also influence the phenotype of the associated macrophages[16]. In other words, the normal foreign body response to an unseeded polymeric scaffold results in worse outcomes. Clearly, therefore, the inflammatory component of neovessel development must be understood and controlled to ensure improved outcomes. A follow-up study documented the time-course of extracellular matrix protein deposition, including elastin and fibrillar collagens, and suggested that the evolving mechanobiological environment in which the infiltrating synthetic cells reside becomes increasingly important as the polymeric scaffold degrades and the neotissue carries more and more of the hemodynamic load[29].

Notwithstanding the fundamental role of experimental studies, computational models can provide additional insight into many aspects of vascular mechanics and biology. Fortunately, considerable progress has been achieved in developing mixture theory-based computational models of growth (changes in mass) and remodeling (changes in microstructure) in tissue engineering[23,38]. In particular, our group developed a constrained mixture model of neovessel development[27] by extending prior models of mechano-adaptations by native blood vessels to sustained alterations in hemodynamic loading[37]. Initial simulations revealed the need to complement mechano-mediated matrix production with an immuno-driven production, consistent with available data. By describing[27] and predicting[19] the evolving mechanical properties of TEVGs, this model proved to be a reliable tool for assessing neovessel development.

Importantly, however, exuberant early inflammation plays a key role in graft narrowing and potential failure[15,22] and our previous computational model was informed by data from

unseeded PGA-P(CL/LA) grafts explanted from SCID/bg mice. Briefly, the severe combined immunodeficiency (SCID) mutation prevents proper development of mature T-cells and B-cells while the beige (bg) mutation affects natural killer (NK) cells, macrophages, platelets, and other myeloid cell activity[25]. Hence, SCID/bg mice have compromised innate and adaptive immune responses. Here, we extend our previous computational model to capture the natural history of *in vivo* TEVG development in both immuno-compromised and immuno-competent mice to delineate better the multiple roles of immuno-driven and mechano-mediated neovessel development from an implanted polymeric scaffold. To complement the prior study, we focus on unseeded grafts that represent a worst case scenario while not introducing another complex variable, namely potential differences in seeding density and cell distributions.

Methods

Scaffold.

TEVGs were constructed from rectangular sheets of PGA felt that were wrapped to form a tube and sealed with a 50:50 copolymer solution of P(CL/LA)[33]. Inner diameter, wall thickness, and axial length were 0.9±0.08 mm, 0.3±0.03 mm, and 3.0±0.23 mm, respectively. Areal density of the PGA felt was 4.5 mg/cm^2. Scanning electron microscopy (SEM) quantified the microstructure of the pre-fabrication PGA felt, at a magnification of 200X, and the luminal surface of the composite PGA-P(CL/LA) graft, at 400X (n=3 samples each, 3 images per sample). These images enabled quantification of initial polymer pore size (r^p) and fiber diameter (ω^p) using a custom MATLAB image segmentation algorithm based on Fuzzy C-means clustering and the diameterJ plug-in for ImageJ (NIH, Bethesda, MD, USA), respectively.

Select scaffolds were incubated *in vitro* in phosphate-buffered saline (PBS, Gibco) at 37°C to allow polymer degradation by hydrolysis; this solution was changed weekly to minimize possible catalytic effects of acidic degradation products. Scaffolds were removed from the PBS at 0, 1, 2, 4, or 6 weeks (n=3 per time) and cannulated for uniaxial force-length testing using a custom device[12]. Luminal pressure was zero during testing since non-implanted scaffolds are not water-tight. After measuring the unloaded length, each scaffold was preconditioned using a single cycle of incremental stretching to 10%, followed by 10 cycles of axial loading and unloading in increments of 1% from the unloaded configuration to an axial stretch of 10%. Axial force and length were measured throughout.

Graft implantation, harvest, and quantification.

Experiments utilizing immuno-competent C57BL/6 wild-type mice were approved by the Institutional Animal Care and Use Committee of Nationwide Children's Hospital and followed standard guidelines. Unseeded TEVGs were implanted as IVC interposition grafts in 8-week old mice using sterile microsurgical techniques as described previously[33]. Graft patency was assessed longitudinally using transabdominal ultrasound (Vevo 2100, VisualSonics, Inc, Toronto, Canada) and 9 patent specimens were harvested for mechanical testing (from the 12 samples that were implanted, 3 at each of the four times): n=3 at 2 weeks, n=1 at 6 weeks, n=2 at 12 weeks, and n=3 at 24 weeks post-implantation. Just prior

to excision, the graft and adjacent IVC were marked *in situ* with 10-0 prolene sutures along their length to enable the *in vivo* axial stretch to be re-approximated during *in vitro* mechanical testing. Grafts from immuno-compromised CB17 SCID/bg mice were studied similarly as reported previously[30].

Specifically, the composite specimens (proximal IVC, graft, and distal IVC) were cannulated and secured to custom drawn, size-matched glass micropipettes with 6-0 suture and a small drop of cyanoacrylate. Cannulated vessels were placed in our custom computer-controlled biaxial testing device within a Hank's Buffered Salt Solution (HBSS, Gibco) and initial dimensions (outer diameter and axial length) were recorded in the unloaded state. Vessels were then stretched to their estimated *in vivo* axial stretch (based on the prolene sutures), equilibrated at 15 mmHg with physiological intraluminal flow for 15 minutes, and preconditioned via 4 cycles of pressurization from 0 to 30 mmHg. Following preconditioning, unloaded dimensions were measured again and the *in vivo* axial stretch of the composite vessel was determined *in vitro* by identifying the stretch at which the measured axial force remained nearly constant while intraluminal pressure changed. Each specimen was subjected to two cycles of pressure-diameter testing from 0 to 30 mmHg at the experimentally determined *in vivo* axial stretch ratio. Pressure, axial force, axial length, and outer diameter were recorded throughout testing. The mean unloaded thickness was measured via image analysis of cross-sections of intact rings excised following testing. TEVGs from CB17 SCID/bg mice were tested and analyzed similarly[30]. Native IVCs from 8-week old C57BL/6 (n=5) and CB17 SCID/bg (n=5) mice served as appropriate controls[21]. Following testing, specimens were fixed in 10% neutral buffered formalin for 24 hours, embedded in paraffin, sectioned serially at 4 μm, and stained with hematoxylin and eosin (H&E). Additional histology was collected at 3 and 10 weeks for the SCID/bg mouse model.

Theoretical framework.

We employed a general constrained mixture model[17] to describe contributions of individual constituents (e.g., polymer, different families of fibrillar collagens) to the overall structure and function of an evolving TEVG (Fig. 1). Briefly, three classes of constitutive relations are postulated[37] for each constituent $\alpha = 1,2, \ldots, N$: stored energy density functions $\widehat{W}^{\alpha}\left(\mathbf{F}^{\alpha}_{n(\tau)}(s)\right)$ describing the mechanical behavior, mass density production functions $m^{\alpha}(\tau) > 0$ for matrix addition, and survival functions $q^{\alpha}(s, \tau) \in [0,1]$ for mass removal, with growth and remodeling (G&R) time $\tau \in [0, s]$ where s is the current time. Hence, $\mathbf{F}^{\alpha}_{n(\tau)}$ describes the finite deformation experienced by constituent α at G&R time s relative to the natural configuration $n(\tau)$ for that constituent at the time of deposition τ.

We solve the associated wall mechanics problem assuming that neovessel development can be represented by a series of quasi-static equilibrium states. Hence, linear momentum balance requires $div\mathbf{t} = \mathbf{0}$ where $\mathbf{t}$ is the Cauchy stress given constitutively by $(det\mathbf{F})\mathbf{t} = 2\mathbf{F}(\partial W/\partial \mathbf{C})\mathbf{F}^{T}$, with stored energy $W = \sum W^{\alpha}$, right Cauchy-Green tensor $\mathbf{C} = \mathbf{F}^{T}\mathbf{F}$, and deformation gradient tensor $\mathbf{F}$, each for the mixture (i.e., evolving polymer-matrix composite). $\mathbf{F}^{\alpha}_{n(\tau)}(s) = \mathbf{F}(s)\mathbf{F}^{-1}(\tau)\mathbf{G}^{\alpha}(\tau)$, where $\mathbf{G}^{\alpha}$ is the deposition stretch tensor through which each new constituent α is incorporated within the extant material (Fig. 1). For more

details on the framework, see[27]. Herein, we consider $N = 12$ basic constituents. Recalling that the scaffold comprises a PGA felt and P(CL/LA) sealant, we model it as mechanically isotropic based on SEM images of the non-implanted scaffolds (with separate parameters denoted $(.)^{p}_{PGA}$ and $(.)^{p}_{P(CL/LA)}$. We let smooth muscle cells ($a = sm$) be the primary mesenchymal cell type, but with inflammatory ($a = i, sm$) or mechano-mediated ($a = m, sm$) phenotypes. Finally, we use a four-fiber family model for two groups of fibrillar collagens ($a = c$) – those produced in response to inflammatory ($a = i, c$) versus mechanical ($a = m, c$) stimuli – described by an axial family, a circumferential family, and two diagonally symmetric families.

Specifically, the stored energy density $W^{a}(s)$ for any structurally significant constituent a was postulated as[27,37]

$$\rho\left(s\right)W^{\alpha}\left(s\right) = \rho^{\alpha}\left(0\right)Q^{\alpha}\left(s\right)\widehat{W}^{\alpha}\left(\mathbf{F}^{\alpha}_{n(0)}\left(s\right)\right) + \int_{0}^{s} m^{\alpha}\left(\tau\right)q^{\alpha}\left(s,\tau\right)\widehat{W}^{\alpha}\left(\mathbf{F}^{\alpha}_{n(\tau)}\left(s\right)\right)d\tau,$$

where $\rho(s)$ is the evolving mass density of the mixture and $\rho^{a}(0)$ is the apparent mass density of constituent a at G&R time 0 (with $\rho^{c}(0) = 0$). The initial survival function for polymer, $Q^{a=p}(s) \in [0,1]$, where $Q^{p}(s) = q^{p}(s, 0)$, is prescribed as a normalized sigmoidal decay consistent with experiments[32],

$$Q^{p}\left(s\right) = \frac{1 + \exp\left(-k^{p}\zeta^{p}\right)}{1 + \exp\left(k^{p}\left(s - \zeta^{p}\right)\right)},$$

where k^{p} is a rate-type parameter and ζ^{p} adjusts the time of onset of rapid mass loss. Data on polymer degradation were gathered from *in vitro* tests, hence we introduced an inflammatory modifier γ^{i}_{D}, whereby $k^{p} = \gamma^{i}_{D}k^{p}_{E}$ and $\zeta^{p} = \zeta^{p}_{E} \Big/ \gamma^{i}_{D}$ with k^{p}_{E} and ζ^{p}_{E} determined experimentally (see below), since degradation accelerates *in vivo* for polymers degrading via hydrolysis. We assume a neo-Hookean stored energy for both polymeric constituents p, namely

$$\widehat{W}^{p}\left(\mathbf{F}^{p}_{n(0)}\left(s\right)\right) = \mu^{p}\left(s\right)\left(\mathrm{tr}\left(\mathbf{C}^{p}_{n(0)}\left(s\right)\right) - 3\right),$$

with $\mu^{p}(s)$ a shear modulus that evolves as the polymer degrades. Microstructural arguments for porous scaffolds suggest that $\mu^{p}\left(s\right) = 0.03E^{p}_{B}\left(1 - \varepsilon^{p}(s)\right)^{2}$, where E^{p}_{B} is a Young's-type modulus for the solid polymer and $\varepsilon^{p}(s)$ is the changing porosity of the scaffold[11]. $\varepsilon^{p}(s)$ was calculated by inverting an equation relating pore size $r^{p}(s)$, fiber diameter $\omega^{p}(s)$, and porosity, namely

$$r^{p}\left(s\right) = \frac{-\sqrt{\pi}}{4}\left(1 + \frac{\pi}{2\ln\left(\varepsilon^{p}\left(s\right)\right)}\right)\omega^{p}\left(s\right),$$

which stems from empirical characterizations[7]. Because polymer is not produced *in vivo*, $m^p(s) = 0$.

Production of mechano-mediated constituents takes the form[27,37],

$$m^m(\tau) = m_h^m\left(1 - \exp(-\tau)\right)\left(1 + K_\sigma^m \Delta\sigma - K_{\tau_w}^m \Delta\tau_w\right),$$

where m_h^m is the homeostatic production rate in native tissue whereas K_σ^m and $K_{\tau_w}^m$ modulate production according to deviations in intramural circumferential stress and wall shear stress from homeostatic targets, respectively. The term $(1 - \exp(-\tau))$, which is not present in native G&R applications, accounts for a delayed cellular infiltration following implantation. Production of inflammation-stimulated constituents takes the form[27],

$$m^i(\tau) = m_h^i\left(1 - \exp(-\tau)\right)K^i(\tau)\delta^\beta\tau^{\beta-1}\exp(-\delta\tau),$$

where, for simplicity, we let the basal inflammatory production rate $m_h^i = m_h^m$ for each similar type of constituent (e.g., immuno-driven or mechano-mediated collagen). Moreover, $K^i(\tau)$ is a gain parameter for a gamma distribution function with δ and β rate and shape parameters, respectively. We let $K^i(\tau) = K_h^i\left(r_p(\tau) / r_n\right) + K_w^i$, where K_h^i is a basal inflammatory gain, $r_p(\tau)$ is the changing pore size of the scaffold, and r_n is a critical pore size above which cellular infiltration occurs; K_w^i is the baseline inflammatory response to the surgical procedure. This term disappears when G&R time s denotes a homeostatic state in which inflammatory matrix production is negligible.

Removal of matrix proceeds according to a first-order kinetic process, namely $q^\alpha(s,\tau) = \exp\left(-\int_\tau^s k^\alpha(t)dt\right)$ where $k^\alpha(t)$ is a rate-type parameter having different functional forms for immuno-driven and mechano-mediated matrix. As before[27], deviations from the homeostatic mechanical state can increase degradation according to $k^m(t) = k_h^m\left(1 + K_D^m(t)\right)$, where the basal mass loss parameter k_h^m is modulated by normalized differences in stretch from homeostatic via $K_D^m(t)$. Inflammatory constituents are similarly susceptible to increased degradation, with $k^i(t) = k_h^i\left(1 + K_D^i(t)\right)$, though $K_D^i(t) = K^i(t) / K_{max}^i$ with K_{max}^i normalizing the degree of increased degradation due to microstructural cues calculated in K^i(t). Again, basal degradation rates of mechano-mediated and inflammatory constituents are set equal $(k_h^i = k_h^m)$.

Finally, we assume a Fung-type exponential stored energy function[9] for matrix deposited within the graft after implantation, namely

$$\widehat{W}^{\alpha}\left(\mathbf{F}^{\alpha}_{n(\tau)}(s)\right) = \frac{c^{\alpha}_{1}(s,\tau)}{4c^{\alpha}_{2}(s,\tau)}\left(\exp\left[c^{\alpha}_{2}\left(s,\tau\right)\left(\lambda^{\alpha}_{n(\tau)}(s)^{2}-1\right)^{2}\right]-1\right),$$

with $\lambda^{\alpha}_{n(\tau)}(s)$ the principal stretch at G&R time s of a cohort produced at time τ. The material parameters evolve as $c^{\alpha}_{1,2}(s,\tau) = c^{\alpha}_{1,2;h}\left(1-\exp\left(-k_c(s-\tau)\right)\right)$ to account for potential densification and cross-linking of the matrix, which is parameterized phenomenologically given the absence of detailed data. Homeostatic values $c^{\alpha}_{1,h}$ and $c^{\alpha}_{2,h}$ are reached after deposited matrix matures according to rate parameter k_c. These homeostatic values can be determined from experimental data in a native vein for mechano-mediated constituents, but constituents arising from an inflammatory stimulus may have distinct mechanical properties. For inflammatory constituents i, we assumed that the parameters were proportional to those for the mechano-mediated constituents m, that is, $c^{i}_{1,h} = \gamma^{i}_{1}c^{m}_{1,h}$ and $c^{i}_{2,h} = \gamma^{i}_{2}c^{m}_{2,h}$.

Parameter Identification.

Microstructural parameters for the PGA and P(CL/LA) scaffold, including pore size $r^{p}(s)$ and fiber diameter $\omega^{p}(s)$, were quantified from SEM images and used to calculate porosity $\varepsilon^{p}(s)$. Bulk Young's-type moduli E^{p}_{B} for the scaffold came from literature values for a solid polymer[5,26].

Other modeling parameters were selected based on prior G&R computations[27] or determined from fits of experimental data using a Surrogate Management Framework-based (SMF) optimization method, described elsewhere[2] and used before to estimate values of G&R parameters[31]. Briefly, SMF is initialized by sampling the parameter space and computing values of an objective function at each sampled point. A surrogate function is then fit to these sampled points, after which the surrogate is searched for potential minima. True function evaluations are used to iteratively update the surrogate and identify a local minimum. Multiple, semi-random initializations in the parameter space during multiple optimization runs helped to identify unique solutions with convergent parameter values.

The sigmoidal degradation parameters for both polymers, k^{p}_{E} and ζ^{p}_{E}, were determined by fitting the uniaxial degradation data using differences between simulated and experimentally calculated forces at each experimental degradation time. These simulations were run using a simplified version of the full G&R code with only polymer present. Material parameters $c^{m}_{1,h}$ and $c^{m}_{2,h}$ for native collagen and smooth muscle were calculated from fits to the pressure-diameter-axial force data collected previously for both mouse models[21], C57BL/6 and SCID/bg. Homeostatic mass production m^{m}_{h} and degradation rates k^{m}_{h} came from the native homeostatic geometry and prior simulations[27,37]. The critical pore size for normalization r_n came from experimental results for macrophages, which identified a range for non-frustrated

infiltration[10]. The basal gain for immuno-driven mass production K_w^i and similarly gain parameters for mechano-mediated production K_σ^m and $K_{\tau_w}^m$ were taken from prior work[27,28].

The other 8 immuno-related parameters in the G&R framework were fit separately to mean values of pressure-normalized diameter and thickness data for the two mouse models (n=9 each). They are: γ_D^i, the change in polymer degradation due to *in vivo* implantation; γ_1^i and γ_2^i, which control differences in mechanical properties of the inflammatory matrix; k_c, the rate parameter regulating collagen maturation; δ and β, the parameters controlling the rate and shape of the inflammatory gamma distribution function; K_h^i, the gain on inflammatory matrix production and degradation; and K_{max}^i, the scaling factor for increased inflammatory matrix degradation (Table 3). All other model parameters were held constant throughout the fitting. The G&R framework was used to calculate the evolving geometry, including *in vivo* thickness and composition of the graft. Simulated pressure-diameter behaviors were evaluated at experimental times to compare to measured data. Fits were determined by minimizing the difference in normalized pressure-diameter behavior and loaded thickness between experimental and simulated results at each experimental time. Hemodynamic conditions in these lumen-matching IVC interposition grafts were assumed constant, with a luminal pressure of 2 mmHg and a wall shear stress of 2 Pa, as before[27,28].

Results

SEM images of the initial PGA felt and the final composite scaffold sealed with P(CL/LA) reveal the percent reduction in pore size with the addition of sealant, though the overall graft retained an open, porous structure (Fig. 2A; Table 1). As seen in the figure, the original nearly uniform distribution of pore sizes reduced dramatically following the addition of sealant, with a final mean pore size of ~11.2 microns. The fibers making up individual pores were also greatly reduced in diameter (Table 1). These composite scaffolds experienced a complete loss of mechanical integrity by 6 weeks during *in vitro* degradation experiments (Fig. 2B). While the degradation parameters and evolving scaffold material properties were calculated as part of the fitting process, the initial mechanical behavior at 0 weeks was predicted based on material properties of PGA and P(CL/LA) from the literature, the calculated porosity of the scaffold from SEM, and microstructural arguments from the literature[11]. See Table 1. Albeit not shown, parameters found from *in vitro* degradation simulations suggested that these grafts would have been less distensible after 2 weeks than were the implanted grafts despite deposition of new matrix in the latter. That is, our results suggest that *in vivo* immuno-driven processes accelerate polymer degradation.

A detailed comparison of mechanical behaviors of the native veins reveals a structurally stiffer behavior under pressurization in SCID/bg compared to C57BL/6 mice[21]. Separate fitting of the pressure-diameter curves for both types of mice (Fig. 3B) further revealed an increased material stiffness in the SCID/bg mouse despite its lower wall thickness and axial stretch. This difference manifested as a leftward shift in the tension-stretch behavior of veins from the SCID/bg mice (not shown). As matrix components are assumed to be deposited in

native veins in response to mechanical cues, material parameters from the associated regression analyses were included as baseline matrix parameters for the G&R simulations (Table 2).

After 24 weeks of implantation, the mechanical behavior of the implanted grafts showed markedly lower distensibility in pressurization tests compared to the native veins for both mouse models (Fig. 3A). Nonetheless, SCID/bg grafts were more similar to their native IVC, with an average normalized diameter of 1.28 for the grafts vs. 1.42 for its native vein, both at 20 mmHg. In contrast, C57BL/6 results revealed an average normalized diameter of 1.10 for the grafts vs. 1.81 for its native vein (Figs. 3A, B), again at 20 mmHg. Figure 3A shows the evolving pressure-diameter behavior at 2, 6, and 12 weeks of implantation. C57BL/6 grafts behaved similar to SCID/bg grafts at 2 weeks, with average normalized diameters of 1.06 and 1.04, respectively, at 20 mmHg. This observation was surprising given that C57BL/6 grafts were thicker (Fig. 3C). SCID/bg grafts exhibited greater distensibility than the C57BL/6 grafts at later times, with the thickness of the latter remaining more than 100 μm greater than that of the former. When compared within groups, C57BL/6 grafts exhibited similar pressure-normalized diameter behaviors at 2, 6, and 12 weeks, with only slight increases in distensibility with progressive remodeling. In contrast, distensibility improved from 2 to 6 weeks in the SCID/bg mice, though with limited differences from 6 to 12 weeks. The primary difference in thickening was a marked early increase in the C57BL/6 grafts; the SCID/bg grafts generally thinned throughout the time course (Fig. 3C).

Many of the non-inflammatory G&R parameters were selected based on prior simulations for SCID/bg mice[27] (Table 2). In contrast, the inflammatory G&R parameters were determined using the SMF and pressure-normalized diameter and thickness data for both mouse models (Table 3). The G&R simulations (Fig. 3A, C) agreed well with experimental data, with $R^2 = 0.82$ for C57BL/6 data and $R^2 = 0.94$ for SCID/bg data. These immuno-related parameters enable one to assess (patho)physiological properties modeled by the constitutive relations. Inflammatory modifiers of the mechanical behavior of the deposited matrix increased the energy stored by inflammatory constituents for a range of relevant stretches, which may reflect a stiffer matrix deposited via immuno-driven processes (Fig. 4A). Both C57BL/6 and SCID/bg grafts were predicted to have inflammatory matrix stiffer than their respective mechano-mediated matrix, but that in the C57BL/6 grafts was greater. This finding was somewhat unexpected since normal mechano-mediated matrix in the native SCID/bg veins was stiffer than that of the C57BL/6 veins.

Simulated maturation of matrix deposited in the SCID/bg grafts occurred rapidly, with 99% of the maximum values of the material properties attained within 1 week (Fig. 4B); that for the C57BL/6 grafts occurred over a longer period, with 99% of the maximum reached after 20 weeks of remodeling. In combination with the differences in inflammatory modifiers for matrix properties, these simulations suggested a greater capacity to store elastic energy in C57BL/6 than in SCID/bg grafts, at a fixed stretch of 1.08, after 4 weeks (Fig. 4C). It thus appears that while inflammatory matrix is ultimately stiffer in the C57BL/6 mice, a period of remodeling is needed to reach the maximum value. In contrast, inflammatory matrix in the SCID/bg mice appeared to remodel quickly to its final, less stiff, state.

Simulated polymer degradation occurred on similar time scales for both mouse models, with a 0.001 residual volume fraction after 4 weeks, though the P(CL/LA) sealant degraded somewhat earlier in C57BL/6 grafts than in SCID/bg grafts (Fig. 4D). Scaffold fragmentation likely occurred in both models before significant neotissue deposition and cross-linking, similar to previous *in vitro* findings[8], reflected herein by a 2-week graft behavior that was less stiff than that of the non-implanted scaffold. Matrix deposited in response to the inflammatory stimulus degraded more quickly than that in response to the mechanical stimulus, though there were only minor differences in degradation rates for the inflammatory matrix in the two mouse models (Fig. 4E). There were, however, dramatic differences in the gain parameters for inflammatory matrix production between the two models (Fig. 4F). C57BL/6 simulations exhibited an early peak in the gain parameter, within 3 days of implantation, followed by a decay to 0.01 (i.e., less than 1% of baseline value) after ~7 weeks. The gain parameter for the SCID/bg peaked after 5 weeks, with an eventual decay to 0.01 after 22 weeks. Peak values were 27.75 and 5.45 for the C57BL/6 and SCID/bg grafts, respectively, a 5-fold difference. Associated temporal changes were also different between mouse models, with a left-skewed distribution for the C57BL/6 grafts but a nearly normal distribution for the SCID/bg grafts. The rapid increase in matrix production exceeded the loss of scaffold material in the C57BL/6 model, leading to a marked thickening by two weeks. The staggered thickness changes evident in the first two weeks of the SCID/bg model resulted from a different onset of degradation by each of the two polymeric constituents (felt and sealant) along with a delayed production of immuno-driven matrix.

H&E staining of explanted grafts revealed cases of excessive thickening for C57BL/6 grafts that were not seen in SCID/bg grafts (Fig. 5A). Narrowing was observed in both mouse models at the earliest times of histological analysis, though the C57BL/6 graft narrowed more. In all cases of patency at 24 weeks, the lumen increased by 6 weeks as the wall thinned. Scaffolds were infiltrated by cells throughout the full thickness in each mouse model at all times examined (2 to 24 weeks).

Predicted values of normalized radial compliance, an important clinical metric, showed vastly reduced values in C57BL/6 grafts compared with the native C57BL/6 vein at each experimental time (Fig. 5B). Slight increases were seen in C57BL/6 graft compliance as thinning accompanied matrix remodeling over time, but compliance at 24 weeks remained well below the native value. For SCID/bg grafts, compliance increased to near native levels after 24 weeks of remodeling, though a lower compliance was predicted from 6 to 12 weeks due to the delayed onset and peak in the inflammatory gain parameter (Fig. 4F). Note, too, that the native compliance of the C57BL/6 vein is ~2.8 times that of the SCID/bg vein, whereby similar matrix degradation rates in the two mouse models effectively reduce the structural stiffness in the SCID/bg grafts to better match their native compliance at 24 weeks.

Finally, key mechanobiological metrics for G&R simulations of blood vessels generally include pressure-induced circumferential wall stress and flow-induced wall shear stress. Neither predicted value rose to native targets in these mouse models within 24 weeks (Fig. 5C). Importantly, both a low circumferential stress due to wall thickening and a high wall shear stress due to luminal narrowing would be expected to suppress mechano-mediated

matrix production[37]. Circumferential stress increased more in SCID/bg than in C57BL/6 grafts over the 24-week study, but remained less than 50% of its native value. Wall shear stress approached its native value in the SCID/bg mouse, but would likely have gone below the native value based on its projected slope at 24 weeks.

Discussion

Normal vascular cells are exquisitely sensitive to their local mechanical environment, often changing gene expression to promote mechanical homeostasis[18]. Hence, native blood vessels can often mechano-adapt their geometry (i.e., luminal radius, wall thickness, and axial length), structure (i.e., extracellular matrix), function (e.g., cell phenotype or elastic energy storage capacity), and material properties (e.g., stiffness or strength) in response to sustained changes in blood flow and pressure as well as in certain cases of disease or injury. Computational models of the associated mechanobiology and wall mechanics have captured the evolution of such changes[37,39]. More recently, however, it has become apparent that inflammation can have dramatic effects on G&R of even non-diseased vessels, often in concert with changes in hemodynamics. For example, DOCA-salt and angiotensin II induced hypertension in mice lead to an excessive deposition of adventitial collagen that depends primarily on T-cells[3,13]. There is, therefore, a general need to understand better the roles of the immunobiology and mechanobiology in vascular adaptations and disease progression. Indeed, our first computational simulation of the effects of angiotensin II induced hypertension on the murine aorta confirmed the importance of separately considering immuno- and mechano-stimuli[20].

Prior empirical studies of TEVG development in interposition IVC mouse models reveal critical roles for macrophages in both neovessel development (desired) and graft stenosis (undesired)[15,16,22,34]. As in studies of native vessels, there is a critical need to understand better the immunobiology and mechanobiology when studying TEVG development *in vivo*. Given the clear role of monocytes/macrophages in foreign body responses to biomaterials *in vivo*, there has been increased attention to material selection and methods of fabrication to control macrophage phenotype[4,35]. We adopted a different strategy, however. Rather than contrasting effects of different scaffold materials or designs on the inflammation[28], we used a computational model to contrast, for the first time, simulated long-term *in vivo* responses to the same implanted graft (PGA-P(CL/LA) scaffolds) in immuno-competent and immuno-compromised mice.

Albeit not shown, similar to prior findings[27], our mechano-mediated G&R model alone was unable to capture the observed evolving geometry and material properties of IVC interposition TEVGs in either mouse model. One reason for this finding is that circumferential wall stress and wall shear stress remain below normal levels in the current TEVG (Fig. 5C); hence, a mechano-mediated stimulus alone cannot elicit the requisite level of matrix production (cf. Fig. 1). Indeed, previous simulations in arterial TEVGs identify similar states of low stress[36], though this case is unique in that excessive tissue deposition shields mechano-sensitive cells instead of excessive polymer stiffness alone. Therefore, our model independently suggested the need for an additional stimulus, modeled phenomenologically herein as immuno-driven. As expected, fitting our model to data from

C57BL/6 and SCID/bg grafts required a stronger immune contribution in the former. This difference is particularly evident in the multi-fold higher values of the best-fit parameters for the C57BL/6 grafts (Table 3) and the prediction of a much more rapid and extensive inflammatory contribution (Fig. 4F). Given that macrophage-mediated remodeling is critical for successful neovessel development[15], our results suggest that a delayed, moderate increase in inflammatory mediators may be preferred. A mechanistic, not phenomenological, model would be needed to identify a potentially optimal inflammatory time course, however.

Recent empirical findings on the development of IVC interposition TEVGs in SCID mice revealed few phenotypic differences from wild-type, suggesting that a lack of mature T- and B-cells does not dramatically affect neovessel patency[16]. Recalling that the beige (bg) mutation affects myeloid cells, the same investigative group showed that neovessel development could be improved via either antibody neutralization of the NK cells or anti-platelet treatment. By inference, the simulated delay and decrease in inflammatory matrix production in the SCID/bg grafts herein (Fig. 4F) may reflect mainly the bg mutation and its attenuation of cytokine/protease secretion by platelets and macrophages or immune functions by NK cells. Indeed, pilot studies in C57BL/6 grafts explanted shortly after implantation confirm increased platelet adhesion and thrombus formation (not shown). When looking at the natural history of wall composition in C57BL/6 grafts, collagen deposition with possible replacement of thrombus material appears as early as 1-week post-surgery[29]. Such early, dramatic changes are consistent with our simulations for the C57BL/6 gain parameter (Fig. 4F). Infiltration of the graft by monocytes/macrophages could drive the conversion of a soft, fibrin-rich thrombus to a stiffer collagen-rich graft, also observed at 2 weeks and reflected by our computational model (Fig. 3A). Interestingly, inhibition of transforming growth factor type 1 receptor I reduces the classically activated macrophages within a graft and leads to better patency rates and thinner grafts without decreasing the number of infiltrating macrophages[22]. Plasmin, which arises in part via activated platelets, can activate latent TGF-β, which in turn could help drive endothelial-to-mesenchymal transition (endo-MT)[24]. Increased secretion of TGF-β can also arise from accumulated platelets[1]. Furthermore, classically activated macrophages secrete multiple pro-inflammatory cytokines that exacerbate endo-MT, creating a feed-forward cycle that promotes graft stenosis[22] (Fig. 5A). Notwithstanding the utility of our phenomenological model of neovessel development, which lumps all immuno-driven stimuli, there is a need for more mechanistic models of immune cell and platelet activity that can be incorporated within our G&R framework and used to delineate contributors to the inflammation.

Finally, the significant cellularity and matrix accumulation in the SCID/bg grafts highlights a potentially complementary role that a moderate immune response can have on the requisite graded transferal of load-carrying responsibility from the initial polymeric scaffold to the native matrix (Fig. 1), particularly if excessive stiff matrix production can be prevented. Although matrix stiffness appears greater in the native vein of CB17 SCID/bg mice compared to C57BL/6 mice, the immuno-driven collagen production in the C57BL/6 grafts resulted in stiffer fibers than those in the SCID/bg grafts (Fig. 4A). Together these observations suggest that intrinsic differences in immune pathways could contribute to the different values of stiffness in the two mouse models. Of course, differences in mouse background (C57BL/6 vs. CB17) could confound this response, as biomechanical

differences in the wild-type (C57BL/6 vs. CB17) IVC and graft are unknown. Furthermore, the biological mechanism underlying the difference in material stiffness between C57BL/6 and CB17 SCID/bg IVCs has not been identified and could contribute to the observed experimental outcome in ways not predicted by the model. Specifically, SCID/bg mice have deficient adaptive and innate immune systems, and contributions of other immune cells may not be represented well here.

In conclusion, we showed that a single computational model can account for different levels of immuno-driven and mechano-mediated neotissue formation over long periods in TEVGs. Moreover, our data-driven model supports the hypothesis that increased inflammation can lead to stiffer, thicker grafts. Potential advantages of this model are that, given its descriptive capability, it now has potential to be used for hypothesis testing, scaffold design, and potentially the evaluation of adjuvant therapies.

Acknowledgments

This work was supported by grants from the US NIH (R01s HL098228, HL128602, and HL128847 plus MSTP TG T32GM07205), a Pre-doctoral Fellowship from the AHA and Children's Heart Foundation (RK), and a Graduate Student Research Fellowship from the NSF (JMS, NSF DGE1122492).

References

1. Assoian RK, Komoriya A, Meyers CA, Miller DM, Sporn MB. Transforming growth factor-beta in human platelets. Identification of a major storage site, purification, and characterization. J. Biol. Chem 1983 258:7155–7160. [PubMed: 6602130]
2. Audet C, Dennis JE, Jr.. Mesh adaptive direct search algorithms for constrained optimization. SIAM J. Optim 2006 17:188–217.
3. Bersi MR, Khosravi R, Wujciak AJ, Harrison DG, Humphrey JD. Differential cell-matrix mechanoadaptations and inflammation drive regional propensities to aortic fibrosis, aneurysm or dissection in hypertension. J. R. Soc. Interface 2017 14:20170327. [PubMed: 29118111]
4. Brown BN, Ratner BD, Goodman SB, Amar S, Badylak SF. Macrophage polarization: an opportunity for improved outcomes in biomaterials and regenerative medicine. Biomaterials. 2012 33:3792–3802. [PubMed: 22386919]
5. Cohn D, Salomon AH. Designing biodegradable multiblock PCL/PLA thermoplastic elastomers. Biomaterials. 2005 26:2297–2305. [PubMed: 15585232]
6. Drews JD, Miyachi H, Shinoka T. Tissue-engineered vascular grafts for congenital cardiac disease: Clinical experience and current status. Trends Cardiovasc. Med 2017 27:521–531. [PubMed: 28754230]
7. Eichhorn SJ, Sampson WW. Statistical geometry of pores and statistics of porous nanofibrous assemblies. J. R. Soc. Interface 2005 2:309–318. [PubMed: 16849188]
8. Engelmayr GC, Sacks MS. Prediction of extracellular matrix stiffness in engineered heart valve tissues based on nonwoven scaffolds. Biomech. Model. Mechanobiol 2008 7.4:309. [PubMed: 17713801]
9. Ferruzzi J, Vorp DA, Humphrey JD. On constitutive descriptors of the biaxial mechanical behaviour of human abdominal aorta and aneurysms. J. R. Soc. Interface 2010rsif20100299.
10. Garg K, Pullen NA, Oskeritzian CA, Ryan JJ, Bowlin GL. Macrophage functional polarization (M1/M2) in response to varying fiber and pore dimensions of electrospun scaffolds. Biomaterials. 2013 34:4439–4451. [PubMed: 23515178]
11. Gibson LJ, Ashby MF. Cellular solids: structure and properties. 1999 Cambridge University Press, Cambridge.

12. Gleason RL, Gray SP, Wilson E, Humphrey JD. A multiaxial computer-controlled organ culture and biomechanical device for mouse carotid arteries. J. Biomech. Eng 2004 126:787–795. [PubMed: 15796337]
13. Guzik TJ, Hoch NE, Brown KA, McCann LA, Rahman A, Dikalov S, Goronzy J, Weyand C, Harrison DG. Role of the T cell in the genesis of angiotensin II–induced hypertension and vascular dysfunction. J. Exp. Med 2007 204:2449–2460. [PubMed: 17875676]
14. Hibino N, McGillicuddy E, Matsumura G, Ichihara Y, Naito Y, Breuer CK, Shinoka T. Late-term results of tissue-engineered vascular grafts in humans. J. Thorac. Cardiovasc. Surg 2010 139:431–436. [PubMed: 20106404]
15. Hibino N, Yi T, Duncan DRet al.A critical role for macrophages in neovessel formation and the development of stenosis in tissue-engineered vascular grafts. FASEB J. 2011 25:4253–4263. [PubMed: 21865316]
16. Hibino N, Mejias D, Pietris N, Dean E, Yi T, Best C, Shinoka T, Breuer CK. The innate immune system contributes to tissue-engineered vascular graft performance. FASEB J. 2015 29:2431–2438. [PubMed: 25713026]
17. Humphrey JD, Rajagopal KR. A constrained mixture model for growth and remodeling of soft tissues. Math. Models. Methods. Appl. Sci 2002 12:407–430.
18. Humphrey JD. Vascular adaptation and mechanical homeostasis at tissue, cellular, and sub-cellular levels. Cell Biochem. Biophys 2008 50:53–78. [PubMed: 18209957]
19. Khosravi R, Miller KS, Best CA, Shih YC, Lee YU, Yi T, Shinoka T, Breuer CK, Humphrey JD. Biomechanical diversity despite mechanobiological stability in tissue engineered vascular grafts two years post-implantation. Tissue Eng. Part A 2015 21:1529–1538. [PubMed: 25710791]
20. Latorre M, Humphrey JD. Modeling mechano-driven and immuno-mediated aortic maladaptation in hypertension. Biomech. Model. Mechanobiol 2018accepted.
21. Lee YU, Naito Y, Kurobe H, Breuer CK, Humphrey JD. Biaxial mechanical properties of the inferior vena cava in C57BL/6 and CB-17 SCID/bg mice. J. Biomech 2013 46:2277–2282. [PubMed: 23859752]
22. Lee YU, Ruiz-Rosado J. de Dios, Mahler Net al.TGF-β receptor 1 inhibition prevents stenosis of tissue-engineered vascular grafts by reducing host mononuclear phagocyte activation. FASEB J. 2016 30:2627–2636. [PubMed: 27059717]
23. Lemon G, King JR, Byrne HM, Jensen OE, Shakesheff KM. Mathematical modelling of engineered tissue growth using a multiphase porous flow mixture theory. J. Math. Biol 2006 52:571–594. [PubMed: 16463188]
24. Lyons RM, Gentry LE, Purchio AF, Moses HL. Mechanism of activation of latent recombinant transforming growth factor beta 1 by plasmin. J. Cell Biol 1990 110:1361–1367. [PubMed: 2139036]
25. McVey Ward D, Griffiths GM, Stinchcombe JC, Kaplan J. Analysis of the lysosomal storage disease Chediak–Higashi syndrome. Traffic. 2000 1:816–822. [PubMed: 11208072]
26. Middleton JC, Tipton AJ. Synthetic biodegradable polymers as orthopedic devices. Biomaterials. 2000 21:2335–2346. [PubMed: 11055281]
27. Miller KS, Lee YU, Naito Y, Breuer CK, Humphrey JD. Computational model of the in vivo development of a tissue engineered vein from an implanted polymeric construct. J. Biomech 2014 47:2080–2087. [PubMed: 24210474]
28. Miller KS, Khosravi R, Breuer CK, Humphrey JD. A hypothesis-driven parametric study of effects of polymeric scaffold properties on tissue engineered neovessel formation. Acta Biomater. 2015 11:283–294. [PubMed: 25288519]
29. Naito Y, M. Williams-Fritze, Duncan DR, Church SN, Hibino N, Madri JA, Humphrey JD, Shinoka T, Breuer CK. Characterization of the natural history of extracellular matrix production in tissue-engineered vascular grafts during neovessel formation. Cells Tissues Organs. 2012 195:60–72. [PubMed: 21996715]
30. Naito Y, Lee YU, Yi T, Church SN, Solomon D, Humphrey JD, Shinoka T, Breuer CK. Beyond burst pressure: initial evaluation of the natural history of the biaxial mechanical properties of tissue-engineered vascular grafts in the venous circulation using a murine model. Tissue Eng. Part A 2013 20:346–355. [PubMed: 23957852]

31. Ramachandra AB, Sankaran S, Humphrey JD, Marsden AL. Computational simulation of the adaptive capacity of vein grafts in response to increased pressure. J. Biomech. Eng 2015 137:031009.
32. Reed AM, Gilding DK. Biodegradable polymers for use in surgery—poly (glycolic)/poly(Iactic acid) homo and copolymers: 2. In vitro degradation. Polymer. 1981 22:494–498.
33. Roh JD, Nelson GN, Brennan MPet al.Small-diameter biodegradable scaffolds for functional vascular tissue engineering in the mouse model. Biomaterials. 2008 29:1454–1463. [PubMed: 18164056]
34. Roh JD, R. Sawh-Martinez, Brennan MPet al.Tissue-engineered vascular grafts transform into mature blood vessels via an inflammation-mediated process of vascular remodeling. Proc. Natl. Acad. Sci. USA 2010 107:4669–4674. [PubMed: 20207947]
35. Sridharan R, Cameron AR, Kelly DJ, C.J. Kearney, O'Brien FJ. Biomaterial based modulation of macrophage polarization: a review and suggested design principles. Mater. Today 2015 18:313–325.
36. Szafron JM, Breuer CK, Wang Y, Humphrey JD. Stress Analysis-Driven Design of Bilayered Scaffolds for Tissue-Engineered Vascular Grafts. J. Biomech. Eng 2017 139:121008.
37. Valentín A, Cardamone L, Baek S, Humphrey JD. Complementary vasoactivity and matrix remodeling in arterial adaptations to altered flow and pressure. J. R. Soc. Interface 2009 6:293–306. [PubMed: 18647735]
38. Vernerey FJ. A mixture approach to investigate interstitial growth in engineering scaffolds. Biomech. Model. Mechanobiol 2016 15.2:259–278. [PubMed: 26047777]
39. Wilson JS, Baek S, Humphrey JD. Importance of initial aortic properties on the evolving regional anisotropy, stiffness and wall thickness of human abdominal aortic aneurysms. J. R. Soc. Interface 2012rsif20120097.

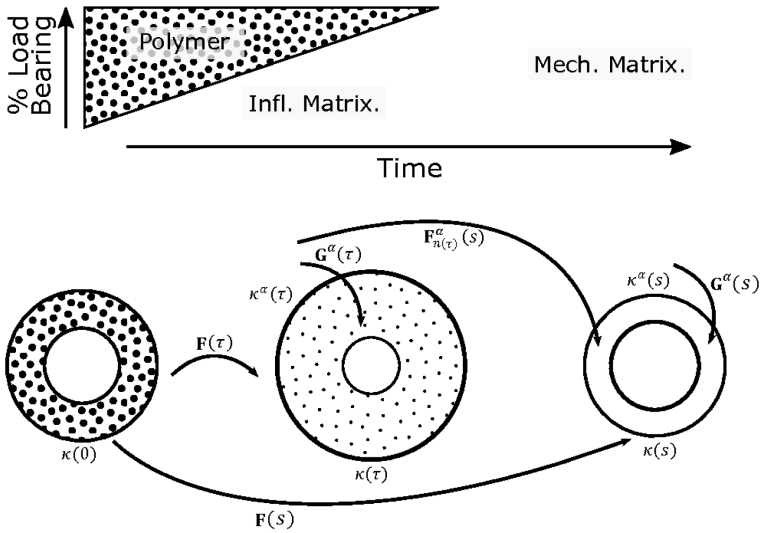

Fig. 1.

(Top) Illustration of an idealized graded transferal of mechanical loads from the degrading polymer to newly deposited extracellular matrix driven by inflammation (infl.) and mediated by mechanical stimuli (mech.). (Bottom) Three configurations important to G&R of a constrained mixture. Polymer alone exists in the initial configuration $k(0)$, while at later times $\tau \in (0, s)$ the graft is in configuration $k(\tau)$ and immuno-driven and mechano-mediated matrix are deposited relative to natural configurations $k_n^{\alpha}(\tau)$, which induces a deposition pre-stretch via the linear transformation $\mathbf{G}a(\tau)$. Finally, following depressed immune responses at long times s, mechano-mediated matrix turns over with updated natural configurations and pre-stretches. The deformation of a constituent deposited at time τ and existing at time s is $\mathbf{F}^{\alpha}_{n(\tau)}(s) = \mathbf{F}(s)\mathbf{F}^{-1}(\tau)\mathbf{G}^{\alpha}(\tau)$.

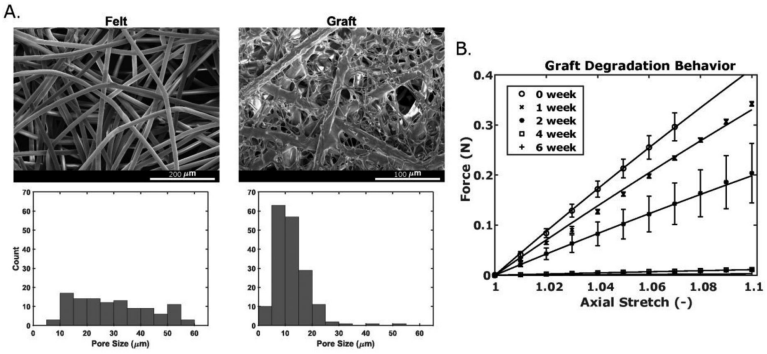

Fig. 2.

(A) Scanning electron microscopic images of the PGA felt (left) and composite PGA-P(CL/LA) graft (right) with respective pore size distributions (below). The composite scaffold is shown at twice the magnification. (B) Uniaxial force is plotted versus axial stretch for *in vitro* graft degradation over six weeks, with experimental data represented symbolically (mean±SEM) and model fits represented as solid lines. Note that the 6-week force-axial stretch data are under the 4-week data.

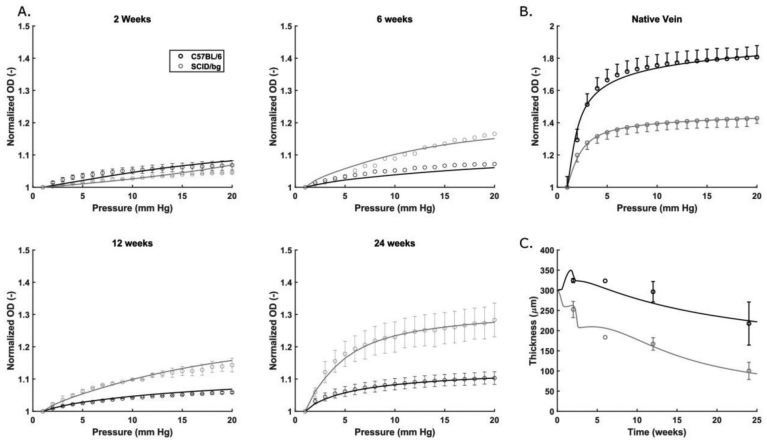

Fig. 3.

Normalized outer diameter (OD) plotted versus luminal pressure for (A) grafts explanted from C57BL/6 (dark) and SCID/bg (light) mice after 2, 6, 12, or 24 weeks and (B) native veins from both mouse models. (C) Evolution of TEVG thickness, at physiological loading, for grafts explanted from both mouse models. In each case, experimental data (mean±SEM) are represented symbolically and model fits as solid lines.

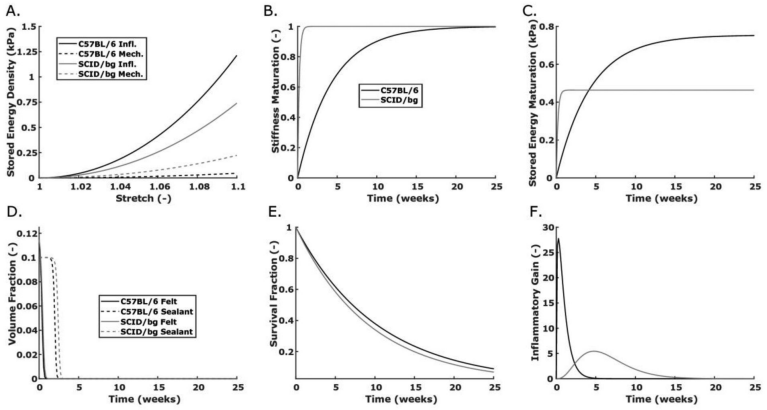

Fig. 4.

Computational predictions for constitutive functions/parameters of interest in the G&R model for C57BL/6 (dark) and SCID/bg (light) mice: (A) stored energy density vs. stretch for immuno-driven (solid) and mechano-mediated (dashed) collagen production, (B) maturation of matrix stiffness vs. time since production, (C) a combined plot of inflammatory stored energy density at a stretch of 1.08 as a function of time since collagen production, (D) polymer constituent volume fractions vs. G&R time, that is, since graft implantation, (E) survival fraction of inflammatory matrix since the time it was produced, and (F) evolving values of the inflammatory gain parameter for matrix production.

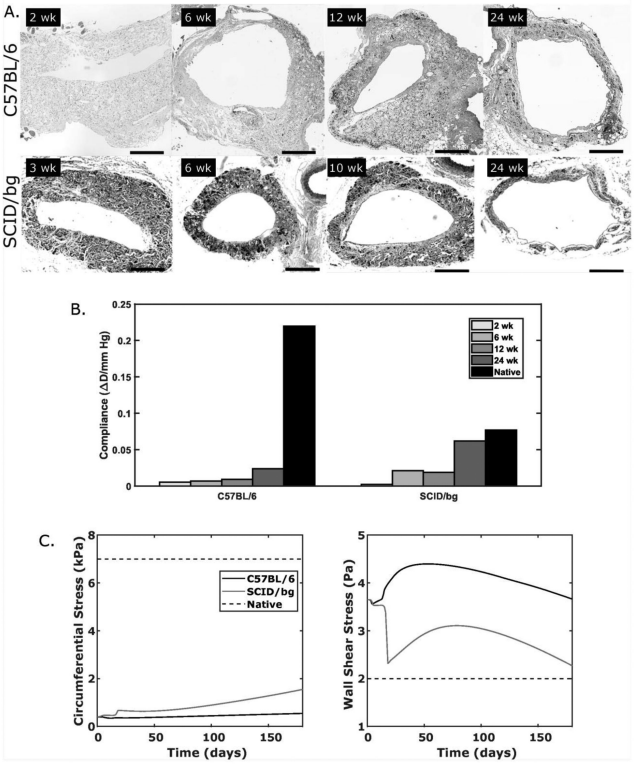

Fig. 5.

(A) Representative micrographs of grafts explanted from C57BL/6 (top) and SCID/bg (bottom) mice over 24 weeks. (B) Predicted values of evolving normalized diameter compliance compared to native compliance over 2 to 3 mmHg. (C) Predicted evolution of pressure-induced circumferential wall stress and flow-induced wall shear stress, which drive mechano-mediated matrix production, for both mouse models as a function of G&R time. Normal, unchanging, values of each are shown as native (dashed).

Table 1.

Parameters for the polymeric scaffold, found from experiments or the literature[5,26,32], which are used as inputs to the computational G&R model.

Parameter	Description	Value	Units
r^p_{PGA}	PGA felt pore size	39.3	μm
ω^p_{PGA}	PGA felt fiber diameter	15.9	μm
E^p_{PGA}	PGA Young's-type modulus[23]	7	GPa
k^p_{PGA}	PGA degradation rate	0.128	1/days
ζ^p_{PGA}	PGA degradation shape parameter	28.5	days
r^p	PGA-P(CL/LA) scaffold pore size	11.2	μm
ω^p	PGA-P(CL/LA) scaffold fiber diameter	4.01	μm
$E^p_{P(CL/LA)}$	P(CL/LA) Young's-type modulus[5]	0.1	GPa
$k^p_{P(CL/LA)}$	P(CL/LA) degradation rate	0.138	1/days
$\zeta^p_{P(CL/LA)}$	P(CL/LA) shape parameter	130.25	days

Table 2.

Parameters for collagen and smooth muscle cells, found from experiments or the literature[27,28], which are used as inputs to the computational G&R model.

Native Vein Mechanical Fitting			
Parameter	**Description**	**Value**	**Units**
$c^{c}_{1,h}$	C57BL/6 collagen material parameter 1	4.2	kPa
$c^{c}_{2,h}$	C57BL/6 collagen material parameter 2	0.1	(−)
$c^{sm}_{1,h}$	C57BL/6 SMC material parameter 1	1.68	kPa
$c^{sm}_{2,h}$	C57BL/6 SMC material parameter 2	0.36	(−)
$c^{c}_{1,h}$	SCID/bg collagen material parameter 1	2	kPa
$c^{c}_{2,h}$	SCID/bg collagen material parameter 2	0.5	(−)
$c^{sm}_{1,h}$	SCID/bg SMC material parameter 1	3.1	kPa
$c^{sm}_{2,h}$	SCID/bg SMC material parameter 2	3.15	(−)
Prior G&R Simulations			
Parameter	**Description**	**Value**	**Units**
$m^{m,c}_{h}$	basal collagen production rate	0.123	mg/(m^2·days)
$k^{m,c}_{h}$	basal collagen degradation rate[34]	1/80	days
$m^{m,sm}_{h}$	basal SMC production rate	0.131	mg/(m^2·days)
$k^{m,sm}_{h}$	basal SMC degradation rate[34]	1/80	days
K^{m}_{σ}	production gain from circumferential stress[24]	1	(−)
$K^{m}_{\tau_w}$	production gain from wall shear stress[25]	5	(−)
K^{i}_{w}	baseline wounding response[25]	5	(−)
r_n	critical pore size[8]	10	μm

Table 3.

G&R model parameters found by fitting the longitudinal pressure-normalized diameter and thickness data for both mouse models.

Parameter	Description	C57BL/6	SCID/bg	Units
γ_D^i	change in polymer degradation	4	3.29	(−)
γ_1^i	inflammatory mechanical modifier	25.5	3.34	(−)
γ_2^i	inflammatory mechanical modifier	12.22	0.43	(−)
k_c	collagen maturation rate parameter	0.71	0.03	1/days
δ	inflammatory distribution rate parameter	0.21	0.09	1/days
β	inflammatory distribution shape parameter	1.38	4	(−)
K_h^i	inflammatory gain	5.08	0.1	(−)
K_{max}^i	inflammatory degradation scaling factor	500	13.013	(−)